PROCEEDINGS A

royalsocietypublishing.org/journal/rspa

Research



Cite this article: Bailey SCC, Canter CA, Sama MP, Houston AL, Smith SW. 2019 Unmanned aerial vehicles reveal the impact of a total solar eclipse on the atmospheric surface layer. *Proc. R. Soc. A* **475**: 20190212. http://dx.doi.org/10.1098/rspa.2019.0212

Received: 9 April 2019 Accepted: 21 August 2019

Subject Areas:

atmospheric science, meteorology, fluid mechanics

Keywords:

atmospheric surface layer, eclipse, measurements, unmanned aerial vehicles, turbulence

Author for correspondence:

Sean C. C. Bailey e-mail: sean.bailey@uky.edu

Unmanned aerial vehicles reveal the impact of a total solar eclipse on the atmospheric surface layer

Sean C. C. Bailey¹, Caleb A. Canter¹, Michael P. Sama², Adam L. Houston³ and Suzanne Weaver Smith¹

¹Department of Mechanical Engineering, and ²Biosystems and Agricultural Engineering, University of Kentucky, Lexington, KY 40506, USA

³Earth and Atmospheric Sciences, University of Nebraska-Lincoln, Lincoln, NE 68588, USA

SCCB, 0000-0002-9807-9858

We use unmanned aerial vehicles to interrogate the surface layer processes during a solar eclipse and gain a comprehensive look at the changes made to the atmospheric surface layer as a result of the rapid change of insolation. Measurements of the atmospheric surface layer structure made by the unmanned systems are connected to surface measurements to provide a holistic view of the impact of the eclipse on the near-surface behaviour, largescale turbulent structures and small-scale turbulent dynamics. Different regimes of atmospheric surface layer behaviour were identified, with the most significant impact including the formation of a stable layer just after totality and evidence of Kelvin-Helmholtz waves appearing at the interface between this layer and the residual layer forming above it. The decrease in surface heating caused a commensurate decrease in buoyant turbulent production, which resulted in a rapid decay of the turbulence in the atmospheric surface layer both within the stable layer and in the mixed layer forming above it. Significant changes in the wind direction were imposed by the decrease in insolation, with evidence supporting the formation of a nocturnal jet, as well as backing of the wind vector within the stable layer.

1. Introduction

As eloquently stated by the seventeenth-century mathematician Evangelista Torricelli, 'we live submerged at the bottom of an ocean of air' [1]. Less prosaically, but perhaps more specifically, we can say that humanity is immersed within the atmospheric boundary layer and therefore our lives are constantly influenced by its dynamics in ways that are both perceptible and imperceptible. The lowest 10% of the atmospheric boundary layer is the atmospheric surface layer, and the turbulence within this portion of the atmosphere enhances the surface layer's impact on atmospheric dynamics. Turbulent transport causes the atmospheric surface layer to act as a sink of both kinetic energy and momentum for the remaining boundary layer, as well as to act as a source of heat, water vapour and other scalars that become transported into the troposphere [2]. Most of this transport is carried out through persistent coherent motions, or 'coherent structures', which populate turbulent flows [3,4].

Turbulence is introduced into the atmospheric surface layer by the boundary conditions at the surface—atmosphere interface. It is the result of both mechanical production, caused by shear stress at the surface, and buoyancy-driven production, caused by temperature and humidity gradients introduced by the difference in thermodynamic properties at the air—surface interface. During summer daylight hours, most of the turbulent production is buoyancy driven, resulting in a convective boundary layer. The surface layer in a convective boundary layer is unstable and highly turbulent, and is dominated by coherent motions in the form of thermals and rising air which enhance vertical mixing throughout the boundary layer. The thermal gradients that cause this buoyant forcing arise as a result of the insolation, or amount of solar radiation, which heats the Earth's surface relative to the neighbouring air. During the typical diurnal cycle, the time scale of this insolation change is long, of the order of 1 h.

During a solar eclipse, the rate of insolation change is more rapid, creating an opportunity to study the dynamics of the atmospheric surface layer under atypical forcing, and making this astronomical event a meteorological one. The phase of an eclipse can be described using the terms first, second, third and fourth contact, which refer to the times at which the eclipse starts, totality starts, totality ends and the eclipse ends, respectively. The time between first contact and second contact, of the order of an hour, can have the same net insolation decrease as would occur from midday to sunset. The amount of insolation change is variable depending on the time of day it occurs, and whether the eclipse is partial or total. For a partial eclipse, there is no second and third contact; instead, one uses the time of maximum obscuration to separate the phases of the eclipse.

As a result of the potential insight into the atmosphere's response to the rate of change in forcing, there have been numerous studies reporting meteorological measurements made during both partial and total eclipse conditions. With the exception of a few remote sensing experiments [5–8], observations of atmospheric surface layer properties have largely been limited to surface observations. Generally, the decrease in insolation which occurs during the eclipse is accompanied by a corresponding decrease in temperature [9–11]. The minimum temperature occurs after third contact, or maximum obscuration, with time lags typically of the order of 10–20 min reported [12–14], although a longer lag of 30 min was reported over the Antarctic [15] and attributed to the reduced insolation at this location. This time lag for the temperature minimum is caused by the difference in thermal inertia between the air and neighbouring surface. Soil temperatures also show a minimum [6,16], with the time lag of the minimum increasing with depth. Along with the temperature decrease of the air comes a commensurate increase in reported relative humidity (RH) [10,11].

Observations of the surface winds indicate less consistent behaviour. Although some studies report a decrease in wind corresponding to the decrease in temperature [9,10,17], others note no change in the surface winds [7]. Increasing wind magnitude coupled with direction changes before and after an eclipse [6,18,19], sometimes referred to as an eclipse wind, have been associated with the formation of a cold-core cyclone [20], as proposed in the early twentieth century [21]. The formation of a cold-core cyclone has been supported in some studies [22,23],

while other studies suggest that anecdotal reports of eclipse winds are due to an enhanced wind chill effect [14].

One of the difficulties in interpreting surface winds, in particular their decrease and change in direction, is the potential suppression of turbulence which may occur due to re-stabilization in the atmospheric surface layer as the surface cools relative to the air [7,10]. Most studies that report surface layer stability measurements indicate that there is an increase in stability of the boundary layer, although both fully stable conditions [6,8,12,24] and marginally unstable conditions [8,9, 16,25] have been reported to occur during the eclipse. When stable conditions are reported, they persist for as long as 45 min after maximum obscuration [6,7,13].

Such stabilization of the atmospheric surface layer is expected to cause a corresponding reduction in the atmospheric boundary layer height [10] due to suppression of the vertical motions and rising thermals which drive the boundary layer vertically. The suppression of these vertical motions is consistent with remote sensing observations reporting a reduction in boundary layer height [8,26], and a reduction in the frequency of surface plumes [5]. Other eclipse effects observed in the upper atmospheric boundary layer include the formation of a temperature inversion at 2000 m [18] and the formation of Kelvin–Helmholtz waves at a similar height [6]. Commensurate with increasing atmospheric surface layer stability are measurements of turbulence, indicating significant decay in the near-surface atmospheric surface turbulence [9,17,18,24,25,27,28], with turbulence decay observed throughout the depth of the boundary layer [7].

Clearly, the dynamics of the atmospheric surface layer change dramatically during a solar eclipse. However, understanding of these changes is limited by a dependence on surface observations and a lack of knowledge about the evolution of vertical gradients in the surface layer. This is caused by a gap in our ability to interrogate the region between surface measurements (typically, less than 10 m in height) and the lower limits of remote sensing tools (e.g. data from between 50 and 200 m up to 2000 m). Recently, unmanned aerial vehicles (UAVs) have been increasingly implemented to address this gap in the altitude range and conduct measurements of the atmospheric surface layer. Although fixed towers can provide data in this range, these towers are limited to sparsely located meteorological sites and have very limited portability. In this respect, UAVs offer distinct advantages over fixed towers for measurements of highly transient and rare events, such as an eclipse. In addition, within the short time scales of the eclipse a UAV can collect substantially more wind and turbulence data than fixed-point measurements, owing to their ability to sample spatially as well as temporally.

As mentioned above, the use of aerial vehicles for meteorological studies is not new. Manned aircraft have been used to conduct atmospheric research for decades, conducting weather reconnaissance; measuring mean wind, temperature and humidity profiles; measuring atmospheric turbulence; and tracking pollutant concentrations [29–44]. Because of their ability to safely perform measurements within metres of the surface and through greatly reduced operational costs [45], the use of UAVs for atmospheric turbulence research is developing rapidly. UAVs have been used to supplement traditional instrumentation in the study of a diverse range of topics including boundary layer evolution [46–53], aerosols and gas concentrations [54–56], cloud microphysics [57] and turbulence [58,59].

The study reported here was conducted in Russellville, KY, USA, during the total eclipse of 21 August 2017. Several prior studies have reported observations from this eclipse, including a detailed diagnosis of the atmospheric boundary layer response by Turner *et al.* [60], who observed turbulent kinetic energy decay and the formation of a stable boundary layer during and after the eclipse. In addition, surface flux measurements by Wood *et al.* [61] over different surfaces found evidence of stable conditions and turbulence suppression during and after totality, with a corresponding decrease in latent and sensible heat flux. Radiosonde measurements have also been reported, with the objective of measuring stratospheric gravity waves [62], and pressure, temperature and humidity profiles measured by a UAV compared with large-eddy simulations of the eclipse event [63]. This article presents the results from multiple, instrumented UAVs measuring within the atmospheric surface layer to resolve the dynamics of the turbulence and

coherent motions as they respond to the rapid insolation changes which occur during a total eclipse. In addition to being within the path of totality, at this location first contact initiated at 11.58 Central Daylight Time (CDT), when the insolation during the uninterrupted diurnal cycle is at a maximum, and hence also the impact of the eclipse. All times provided are in local time, i.e. CDT. On this day, the sky was virtually cloudless, further maximizing the response of the atmospheric surface layer to the eclipse.

2. Experiment description

(a) Overview of measurement

The measurements were conducted at the Russellville–Logan County Airport (36.797326° latitude, -86.812341° longitude, 210 m a.s.l) located 6 km to the southeast of Russellville, KY, USA. The measurement area is shown in figure 1. The airport is surrounded by heterogeneous land use, mostly consisting of farmland with associated scattered stands of trees and ponds within a 5 km radius of the airport. A larger stand of trees was located 1.5 km to the north of the airport. Mean winds for the day reported in METAR data from the nearby Bowling Green Airport were $1.4\,\mathrm{m\,s^{-1}}$ from the SSW, with mean temperatures of $27^{\circ}\mathrm{C}$, sea-level pressure of $102.0\,\mathrm{kPa}$, and mean humidity of 71%.

First contact at this location occurred at 11.58 CDT, second contact at 13.26 CDT, third contact at 13.28 CDT and fourth contact at 14.53 CDT. Measurements were conducted between approximately 9.00 CDT and 15.00 CDT using five different types of systems. These systems consisted of two BLUECAT5 fixed-wing UAVs, one SOLO rotorcraft UAV, a portable weather station, ground temperature sensors and a sonic anemometer. The location of each system is indicated in figure 1.

The portable weather station logged continuously at $1\,\mathrm{Hz}$ from $9.20\,\mathrm{CDT}$ to $14.57\,\mathrm{CDT}$. Ground temperature data were logged at $1\,\mathrm{Hz}$ between $9.08\,\mathrm{CDT}$ and $15.19\,\mathrm{CDT}$. The sonic anemometer was mounted on a $7\,\mathrm{m}$ tower with data logged continuously from $9.33\,\mathrm{CDT}$ to $15.00\,\mathrm{CDT}$ at $100\,\mathrm{Hz}$

The two BLUECAT5 fixed-wing UAVs were flown simultaneously at 50 m and 100 m above ground level (AGL). Each flight consisted of repeatedly traversing the same 800 m long straight line transect at $20\,\mathrm{m\,s^{-1}}$, indicated on figure 1, with typically 40 transects made per flight in alternating directions with 50 s between each transect while the aircraft turned around. After approximately 40 min of flight time, the aircraft were recovered, data downloaded and batteries changed, making the aircraft ready for the next flight. Five of these multi-aircraft flights were conducted, approximately once per hour, between 10.20 CDT and 14.45 CDT.

The SOLO rotorcraft UAV was flown between 10.23 CDT and 14.39 CDT. This aircraft was operated above the sonic anemometer, flying vertical ascents and descents at $2\,\mathrm{m\,s^{-1}}$ between 10 m and 100 m. Up to 10 ascent/descent combinations were flown in a single flight before the aircraft's batteries required changing. Once the batteries were changed, the aircraft was returned to flight. Fifteen of these flights were flown during the measurement day, with times between flights depending on battery availability and charge rates, with most flights separated by less than 5 min but flights 8 and 9 separated by 37 min.

The following subsections describe each measurement system in detail, with post-processing procedures described in appendix A.

(b) Fixed-wing aircraft

Two BLUECAT5 fixed-wing aircraft were used to measure turbulence statistics during the measurement period. These aircraft are described in detail in Witte *et al.* [59] and only briefly described here. They were built around the commercially available flying wing Skywalker X8 airframe, heavily modified for atmospheric measurements. BLUECAT5 offered flight times of



Figure 1. Satellite imagery of the region upwind of the measurement location, showing the location of the different instruments used in the experiment. (Online version in colour.)

close to $45 \,\mathrm{min}$ at $20 \,\mathrm{m\,s^{-1}}$ cruise speeds and could be bungee launched and recovered via skid landing for operations in unprepared sites.

The airframe was equipped with a 3DR Pixhawk commercial autopilot for waypoint-following flight. The UAV was equipped with a 30 cm long, 3.175 mm diameter brass RCATS-120 Pitot-static tube produced by RCATS Systems to provide the autopilot with an accurate true airspeed reading needed to maintain controlled flight. In addition, the Pitot-static tube was used to provide a reference static pressure for the turbulence measurement system. The true airspeed information was also used in the data reduction as a reference velocity signal for cross-correlating the autopilot telemetry signal with the turbulence measurement system velocity signal. This Pitot tube was mounted 25 cm in front of the nose of the aircraft away from the fuselage, 3 cm below the five-hole probe. The transducer used with the Pitot-static tube and autopilot was acquired using a Freescale Semiconductor mpxv7002dp differential pressure transducer with a 2 kPa range.

Six degrees of freedom position and rate information was provided by a VN-300 manufactured by VectorNav. The VN-300 provided a heading accuracy of 0.3° and pitch/roll accuracy of 0.1° with ground velocity accuracy of $\pm 0.05\,\mathrm{ms^{-1}}$. The inertial navigation system also was capable of an increased sample rate of up to $400\,\mathrm{Hz}$ for all variables; however, a $200\,\mathrm{Hz}$ sample rate was used for the experiments. The software required to run the VN-300 was installed on an on-board personal computer.

To measure turbulence in the atmospheric boundary layer, each BLUECAT5 UAV was equipped with a five-hole probe, pressure transducers and data acquisition unit controlled by the on-board computer. The five-hole probe was manufactured in-house with pressure measurements acquired using 4515-DS5A002DP (TE Connectivity, Switzerland) differential pressure transducers with a 0.5 kPa range. Analogue output from the sensors was digitized at 16-bit resolution using a rate of 4000 kHz to use the transducers' internal 2000 kHz low-pass filter as an anti-aliasing filter.

Before flight, each five-hole probe was calibrated using a $0.6 \,\mathrm{m} \times 0.6 \,\mathrm{m}$ wind tunnel. The calibration followed a standard calibration technique outlined by Treaster & Yocum [64] following the Wildmann *et al.* [65] study, which showed better results than the Bohn & Simon method [66].

An additional calibration was conducted to determine the frequency response of the five-hole probe. The results showed a slightly under-damped response, with a corresponding frequency response of 100 Hz. At the typical cruise speed of BLUECAT5, this frequency response translates to a spatial measurement resolution of approximately 0.2 m. Interference effects between the airframe and five-hole probe were mitigated by placing the probe measurement volume 18 cm in front of the nose of the aircraft, as determined via wind tunnel analysis.

To measure temperature and humidity during flight, an iMet-XQ UAV (Intermet Systems, USA) sensor was used. The iMet humidity sensor supports a full 0–100% RH range at $\pm 5\%$ RH accuracy with a resolution of 0.7% RH. The on-board temperature sensor provides a $\pm 0.3^{\circ}$ C accuracy with a resolution of 0.01°C up to a maximum of 50°C. The response times of these sensors are of the order of 5 and 2 s in still air, respectively, with the iMet-XQ UAV system sampling these sensors at 1 Hz. The iMet-XQ sensor was mounted on top of the aircraft with the thermistor exposed to the airflow but shielded by a three-dimensional printed ABS arch designed to protect it from heating via solar radiation.

All data were logged during flight and analysed *a posteriori*. For the analysis, all data were re-sampled to 200 Hz and aligned in time via cross-correlation of the signals measured by the different systems. The aircraft motion was removed from the measured five-hole-probe relative velocity vector to extract the wind vector using an approach developed for manned aircraft. [67–69]. Further details are available in Witte *et al.* [59].

(c) Rotorcraft

The fixed-wing aircraft measurements were coordinated with measurements from a SOLO quadrotor manufactured by 3DRobotics. The aircraft was equipped with an iMet-XQ UAV sensor, mounted below one of the rotors to ensure sufficient aspiration of the sensors. It was located within a fixture designed to protect it from heating via solar radiation but still allow air flow over the sensor

Wind speed and direction sensing were provided by a TriSonica-Mini sonic anemometer manufactured by Applied Technologies. The anemometer has an acceptance cone for vertical winds of $\pm 20^{\circ}$ to the vertical, which was exceeded during these measurements and therefore only the horizontal wind components are used here. The sonic anemometer was calibrated a posteriori in a $0.6\,\mathrm{m}\times0.6\,\mathrm{m}$ wind tunnel to allow compensation for blockage effects from the sensor housing. The anemometer was mounted on a $0.38\,\mathrm{m}$ carbon fibre post above the main body of the rotorcraft with the optimal height determined by tethered testing in a laboratory. In these tests, the rotors were operated at full speed and the post height adjusted until readings were not affected by additional height adjustments.

Digital output from the sonic anemometer was logged at 10 Hz during flight and analysed *a posteriori* using orientation information from the aircraft's autopilot, also logged at 10 Hz. For the analysis, data from the iMet-XQ sensor were re-sampled to 10 Hz and all signals aligned in time via cross-correlation. The aircraft motion was then removed from the measured sonic anemometer relative velocity vector using the same procedures implemented for the fixed-wing aircraft. For two flights, the first and the ninth, the iMet-XQ failed to log data, and for these flights no humidity data were available and reported temperatures are those output from the sonic anemometer.

(d) Portable weather station

Local variables of pressure, temperature, RH, solar radiation and soil surface volumetric water content were measured by an Onset Computer Corporation HOBO U30 weather station. The weather station was outfitted with an Onset S-BPB-CM50 barometric pressure sensor mounted at 1.8 m, an Onset S-THB-M002 temperature/RH sensor mounted at 2.5 m, an Onset S-LIB-M003 solar radiation sensor mounted at 2.8 m, and an ONSET S-WSB-M003/S-WDA-M003 cup anemometer and direction vane mounted at 3.0 m AGL. An Onset S-SMD-M005 soil moisture sensor was inserted into the first 8 cm of the soil surface. Pressure data were measured at a resolution of 0.01 kPa with an accuracy of ± 0.3 kPa. Temperature data were measured at a resolution of ± 0.02 °C with an accuracy of ± 0.21 °C. RH data were measured at a resolution of 0.1% RH with an accuracy of ± 2.5 % RH. Solar radiation data were measured at a resolution of ± 0.08 % water content with an accuracy of 3.3% water content. Wind speed was measured at a resolution of ± 0.08 % water content with an accuracy of ± 1.1 m s⁻¹, and wind direction was measured at a resolution

of 1.4° with an accuracy of $\pm 5^{\circ}$. All data were logged at 1 Hz. The weather station was powered by a sealed lead-acid battery under continuous charge from a 5 W solar panel. Weather station values were calibrated against the Logan County Kentucky Mesonet station 1.5 m values for the measurement day *a posteriori*.

(e) Sonic anemometer tower

A Model 81 000 ultrasonic anemometer (R.M. Young, USA) provided additional ground-based measurement of wind speed and direction and was mounted on a 7 m tall tower. The Young 81 000 could measure wind speeds of up to $40\,\mathrm{m\,s^{-1}}$ at a resolution of $0.01\,\mathrm{m\,s^{-1}}$ with an accuracy of $\pm 0.05\,\mathrm{m\,s^{-1}}$. Unfortunately, just prior to the measurement day, the vertical component of velocity failed, so only the horizontal (surface parallel) components of velocity were available for measurement.

The temperature provided by the sonic anemometer was calculated based on the speed of sound, leading to a temperature measurement accuracy of $\pm 2^{\circ}$ C. For the data reported here, the anemometer was set to output three analogue voltages digitized at 100 Hz by a standalone high-speed LGR-5329 multifunction data logger (Measurement Computing, USA). Both the anemometer and logger were powered by a single 4S 3300 mAh lithium–polymer battery.

Supplemental temperature and humidity sensors were measured by three type k thermocouples and three Honeywell HH-4000 analogue humidity sensors also mounted on the tower at 3.5, 4.5 and 5.5 m. These data used the factory calibration and averaged to minimize bias errors.

(f) Soil temperature sensors

Soil temperature was monitored using four HOBO MX2303 temperature loggers manufactured by Onset Computer Corporation. The loggers were equipped with two thermocouple temperature probes and had a stated accuracy of $\pm 0.2^{\circ}$ C. The four loggers were placed at four locations in loose, dry soil along a fence line parallel to the fixed-wing aircraft flight path. For each logger, one temperature sensor was placed at a depth of approximately 0.02 m below the surface. The second sensor was placed on the surface of the soil. However, the surface sensors were found to be contaminated by radiative heating and their data were not used. All sensors were calibrated in a laboratory a posteriori using the portable weather station temperature as a reference temperature.

3. Observations

(a) Boundary conditions

The boundary conditions to the atmosphere are reflected in the information recovered from the ground-based sensors during the day of the eclipse, which is presented in figure 2. The clearest indicator of the phase and impact of the eclipse is the measured solar radiation, shown in figure 2a. Typical for a cloudless, summer morning, the solar radiation increases gradually with the Sun's elevation at approximately $2 \text{ W}/(\text{m}^2 \text{ min})$ during the uninterrupted diurnal evolution. The impact of the eclipse is readily evident in an almost linear decrease in measured solar radiation from a peak of 850 W m^{-2} at first contact to 0 W m^{-2} at second contact at a rate of $10 \text{ W}/(\text{m}^2 \text{ min})$. There is no measured radiation during totality, but there is a $10 \text{ W}/(\text{m}^2 \text{ min})$ linear recovery from third contact to fourth contact.

For convenience, we will divide the atmospheric surface layer processes into six different phenomenological regimes, based on the relative behaviour of different contributing terms to the energy balance at the surface, and examine the response of surface parameters within each regime. In figure 2a, the estimated sensible and ground heat flux are presented alongside the solar radiation. Note that these terms are indirect estimates inferred from measured temperatures and are used to infer trends only, with details on how the estimates were obtained provided

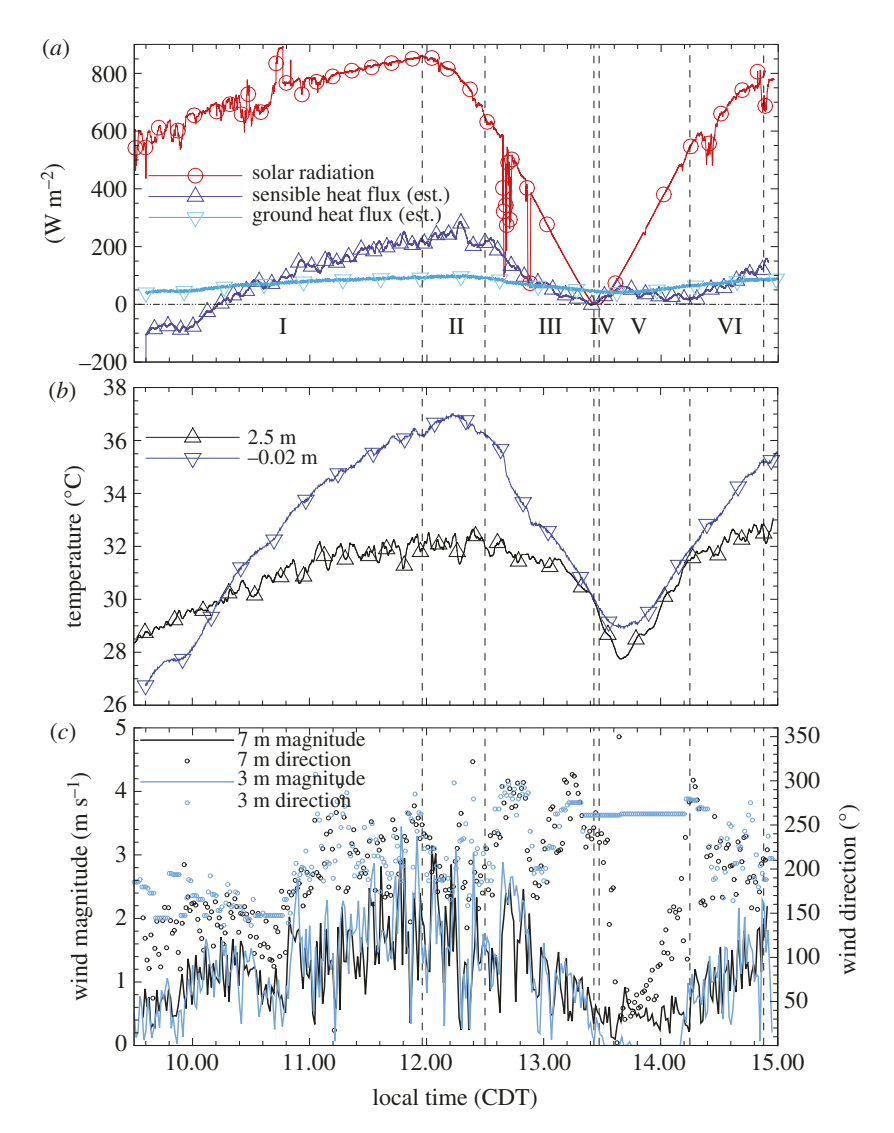


Figure 2. Meteorological conditions measured near the surface. (*a*) Solar radiation measured from 9.30 CDT to 15.00 CDT compared with estimated sensible and ground heat flux inferred for the same time period using measured temperature gradients. (*b*) Air temperature measured at 2.5 m and soil temperature measured at —0.02 m below the surface. (*c*) Wind speed measured at 7 m via a sonic anemometer and at 3.0 m via a cup and vane anemometer. Vectors at the top of the figure indicate the corresponding wind direction, with up being to the North. Vertical dashed lines indicate the boundaries between regimes with regimes identified by Roman numerals in (*a*). (Online version in colour.)

in appendix A. The response at the surface to the eclipse is reflected in the remaining quantities presented in figure 2, specifically temperature (figure 2b) and wind speed and direction (figure 2c). We now examine the behaviour of these quantities for each regime.

Regime I is the unaffected evolution of the boundary layer. As noted above, the solar radiation increased as the day progressed, following the expected behaviour for a typical cloudless morning. Correspondingly, the soil temperature increased and the ground heat flux was into the soil, driven by the relative temperature difference between the soil temperature at the surface and at depth. As the soil temperature increased faster than the air temperature, the soil became warmer than the air shortly after 10.00 CDT. Thus, the sensible heat flux, initially transporting

heat from the air into the soil, transported heat from the surface into the air at increasing rates throughout regime I.

Despite the conduction and turbulent heat flux being away from the surface for the latter half of regime I, the radiative heating of the surface was greater, with the net effect being a gradual increase in the soil temperature throughout regime I at a faster rate than the air temperature increased, resulting in the formation of mixed layer conditions. Correspondingly, the wind speed increased from $1\,\mathrm{m\,s^{-1}}$ to $2.5\,\mathrm{m\,s^{-1}}$ at both $1.5\,\mathrm{m}$ and $7\,\mathrm{m}$.

At first contact, regime II initiated, where all heat fluxes are close to being in balance, resulting in steady-state temperature conditions for both the air and surface. Within this regime, the solar radiation reached a maximum. This resulted in the soil temperature reaching a maximum approximately 12 min past first contact before beginning to decrease as a result of the thermal inertia of the soil. The remaining processes remained approximately constant throughout regime II, with sensible and ground heat flux at their maximums, and away from the surface. Regime II lasted for approximately 30 min before the solar radiation dropped below the combined rate of conduction and turbulent flux away from the surface, and the initiation of regime III.

Lasting until second contact, regime III was characterized by a strong decrease in both soil and air temperatures. This drop was caused by the decrease in solar radiation to zero, yet the surface was still warmer than the air for this regime, sustaining the sensible heat flux into the air until second contact. Although the rate of conduction into the soil reduces, it was still away from the surface. Throughout regime III, the rates at which energy was transferred into and away from the surface decreased significantly relative to regime II. Coinciding with the decrease in sensible heat flux, the wind speed also decreased, with the decrease being slightly faster close to the surface and reaching zero at 3 m, whereas the winds at 7 m remained at 1 m s⁻¹. Along with the drop in the wind speed were very rapid changes in wind direction.

Regime IV occurred between second and third contact and encompassed totality. Within this regime the solar radiation was zero, and the ground surface became equal, or near equal, to the air temperature, cutting off the mechanism driving sensible heat flux. The winds near the surface had calmed, although at $7 \, \mathrm{m}$ they remained at $1 \, \mathrm{m \, s^{-1}}$. Although this wind velocity difference was within the sensitivity of the instruments and therefore insufficient to indicate wind shear at the surface, evidence of a vertical wind shear occurring during this regime is presented in §§3b and d.

Regime V is defined around the region when the soil and air temperature were at minimum, with both the soil and air temperature reaching a minimum at 13.39 CDT, 11 min after third contact. At this time, the solar radiation had increased back to approximately 15% of its first contact value; however, the sensible heat flux remained near zero, with soil and air temperatures very close to each other. The surface continued to lose heat into the soil through conduction, such that the minimum surface temperature reflects the layer of soil near the surface, again storing internal energy after losing it since first contact. Solar radiation increased linearly to 65% of its first contact value throughout regime V; this additional energy added to the surface reversed the loss in surface temperature, and hence the surface temperature increased throughout the remainder of the eclipse. The wind shear initiated at the end of regime III remained throughout regime V, although at the end of regime V the wind at 3 m once again became similar to that measured at 7 m.

We define regime VI as the recovery regime. As the eclipse evolved towards fourth contact, the solar radiation continued to increase and the soil temperature increased accordingly. As a result, within this regime, the sensible heat flux increased rapidly, indicating the resumption of mixed layer conditions and causing an increase in air temperature. Regime VI lasted until fourth contact at 14.53 CDT and the resumption of the undisturbed diurnal cycle.

(b) Atmospheric surface layer structure

The information presented in the previous sections reflects a very dynamic atmospheric surface layer evolution during the eclipse, with changes observed in all measured properties at the

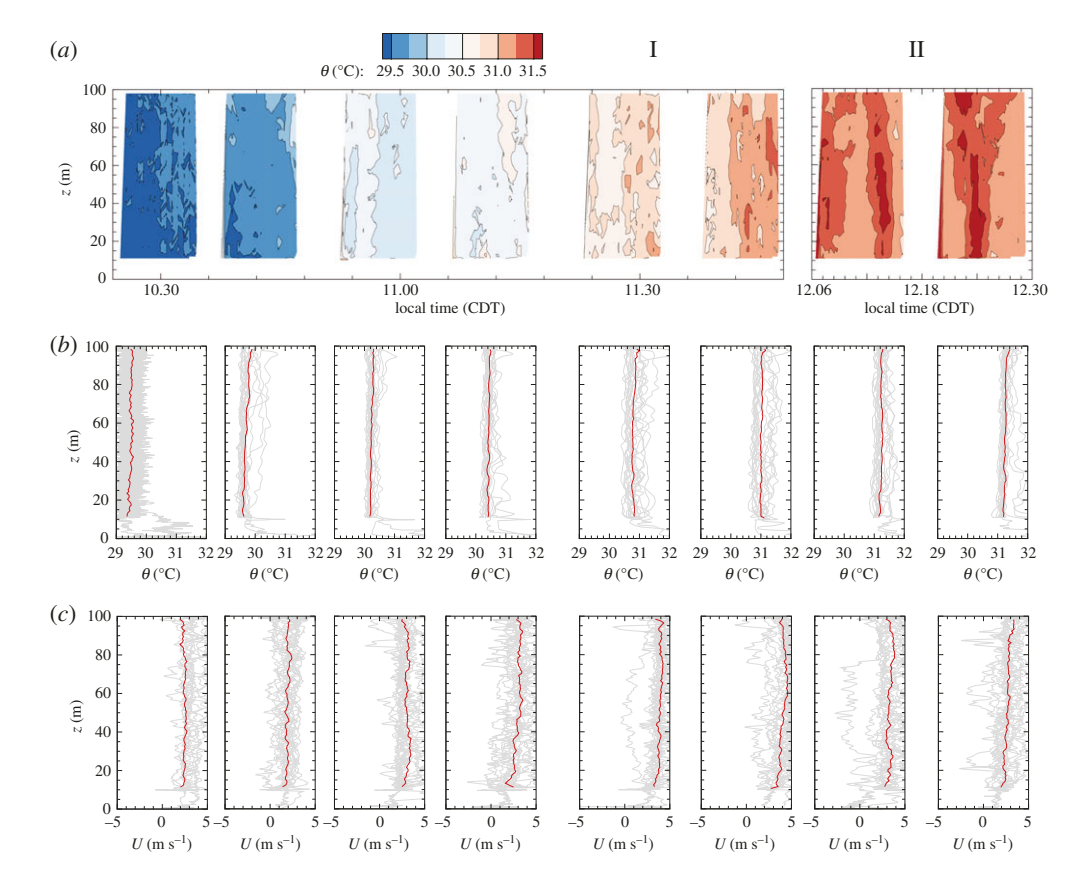


Figure 3. Time evolution of large-scale features of the atmospheric surface layer measured between 10 m and 100 m for regimes I and II. (a) Time—height plot of the potential temperature measured by the profiling UAV interpolated from ascending and descending rotorcraft. Gaps between isocontours indicate the times between flights. (b) Corresponding profiles of potential temperature, θ , from the same data shown in (a). Grey lines indicate the potential temperature measured during ascents and descents of the aircraft with the red line indicating the mean value at each altitude. (c) Profiles of the horizontal component of the wind speed measured from each flight. The coordinate system has been aligned with the average velocity vector calculated from measurements between 50 m and 100 m for each profile. Grey lines indicate the velocity component measured during the ascents and descents with the red line indicating the average value for each flight measured at each 1 m interval height. Vertical lines in (a) indicate the boundaries between regimes, with regimes identified by Roman numerals. (Online version in colour.)

surface. However, without measurements of these properties at higher altitudes, we can only infer the source of many of these changes. The advantages of UAVs become evident in their ability to interrogate a wider range of altitudes within the surface layer than can be accessed via ground instrumentation. With this information, we can connect the regimes established during the discussion of boundary conditions to surface layer dynamics, most notably through the formation and suppression of coherent structures throughout the eclipse evolution. To make this connection, we present isocontours of potential temperature measured during each flight as a function of altitude and time in figures 3a for regimes I and II and 4a for regimes III–VI. We also present the corresponding mean profiles of potential temperature and wind velocity measured during these flights in figures 3b,c and 4b,c, respectively.

As described above, regime I was characterized by the development of mixed layer conditions typical of a cloudless day. The mean profiles of potential temperature (figure 3*b*) and wind (figure 3*c*) all reflect this behaviour, showing little dependence on height above ground as convective structures mix the surface layer vertically. These convective structures can be observed in the potential temperature fields (figure 3*a*) as vertical perturbations which get stronger as

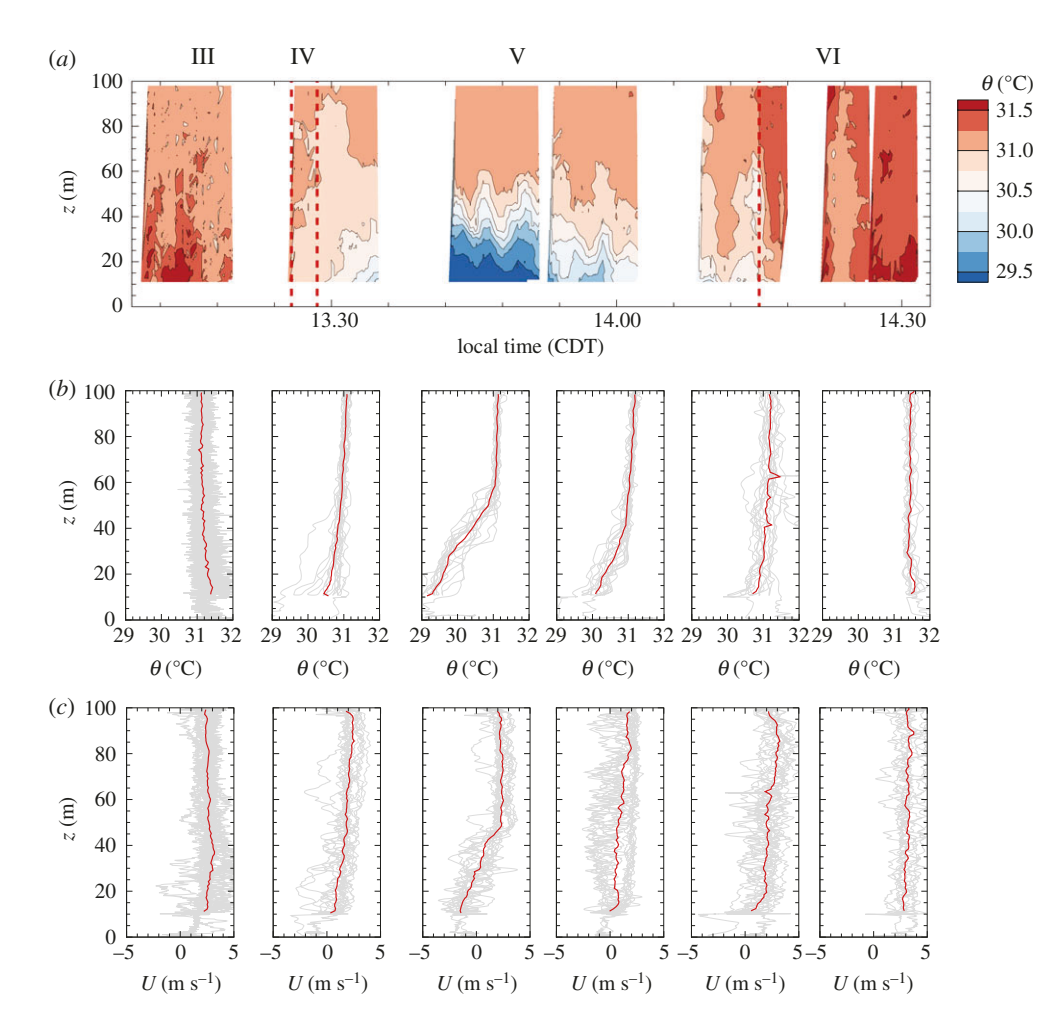


Figure 4. Time evolution of large-scale features of the atmospheric surface layer measured between 10 m and 100 m for regimes III—VI. (a) Time—height plot of the potential temperature measured by the profiling UAV interpolated from ascending and descending rotorcraft. Gaps between isocontours indicate the times between flights. (b) Corresponding profiles of the potential temperature, θ , from the same data shown in (a). Grey lines indicate the potential temperature measured during ascents and descents of the aircraft with the red line indicating the mean value at each altitude. (c) Profiles of the horizontal component of the wind speed measured from each flight. The coordinate system has been aligned with the average velocity vector calculated from the measurements between 50 m and 100 m for each profile. Grey lines indicate the velocity component measured during the ascents and descents with the red line indicating the average value for each flight measured at each 1 m interval height. Vertical lines in (a) indicate the boundaries between the regimes, with regimes identified by Roman numerals. (Online version in colour.)

the temperature difference between the air and surface increases. Similar structures were also observed in the wind and moisture fields (although not shown here). Throughout regime I, the convective structures increased in strength, as measured by the size of the vertical structures and by the potential temperature difference between the structures and their surroundings. These mixed layer conditions continued throughout regimes II and III. During regime II, the convective structures were strongest, fed by a maximization of temperature difference between the air and surface. As the ground and air cooled within regime III the convective behaviour weakened (figure 4a), but mixed layer conditions persisted until second contact.

During regime IV, the convective motions were completely suppressed (figure 4a) and stable conditions began to form, as indicated by a slight temperature inversion near the surface (figure 4b). Corresponding to the increased thermal stability was a decay in the wind speeds near

the surface (figure 4c) as the downward mixing of momentum was shut off by the suppression of convective structures. As a result, winds at the surface were calm, while at $100 \,\mathrm{m}$ they remained largely unchanged from those of regimes I–III.

Regime V was the most dynamic in the surface layer, and thus is the most interesting regime. As a result of the surface temperature reaching its minimum value in this regime, the temperature inversion strengthened, as shown by the mean potential temperature profiles (figure 4b). Such an inversion is analogous to nocturnal surface layer behaviour. Corresponding to the formation of this temperature inversion was the formation of a shear layer in the wind velocity (figure 4c) with flow reversal evident at 20 m between 13.30 CDT and 14.00 CDT. Above the stable layer, the wind speed reduced slightly, but the mean flow largely remained unaffected by changes at the surface. The stable layer grew in time, reaching approximately 50 m in height at 13.45 CDT, when the ground temperature and near-surface air temperature were at a minimum (figure 2b). At this time, there is evidence in figure 4a that waves formed at the interface between the stable layer and the residual layer above it. Note that the period of these waves is approximately 5 min, much greater than the Brunt-Väisälä period, which is estimated to be around 30 s for the temperature gradient and conditions observed during regime V, but of the order of what can be expected for an unstable Kelvin-Helmholtz wavelength corresponding to approximately six times the depth of the shear layer (approx. $300 \,\mathrm{m}$, or $5 \,\mathrm{min}$ if advecting at $1 \,\mathrm{m\,s^{-1}}$). Note that the periodic behaviour was not evident in the 50 m fixed-wing UAV measurements, but we attribute this to the wavelength of these motions being near the Nyquist wavelength of the transect distance. As the surface warmed towards the end of the regime, the temperature inversion weakened and mixed-layer conditions returned, signalling the end of regime V. Thus, regime V represents the formation of a short-lived nocturnal layer, lasting 45 min after third contact.

During regime VI, convective structures are once again evident in figure 4a, driven by the increased thermal gradients at the surface, and mixed layer conditions resume. The convective structures increased in strength towards fourth contact.

(c) Effect of eclipse on the atmospheric surface layer turbulence

The above discussion illustrates the changes which were observed in the large-scale dynamics within the surface layer throughout regimes I–VI. Now, we examine how these large-scale dynamics influenced the surface layer turbulence, as reflected in the turbulence statistics measured by the fixed-wing UAVs flying at 50 m and 100 m and shown in figure 5. Where possible, we also include the same statistics measured at 7 m by the tower-mounted sonic anemometer.

The buoyant forcing by the large-scale convective eddies visualized in figures 3a and 4a can be quantified by the buoyant production term of the turbulent kinetic energy budget, shown in figure 5a. Although it oscillated significantly as a result of large-scale mixing events, the buoyant production displayed a general increase in time, within regime I, producing a corresponding increase in turbulent kinetic energy. The turbulent kinetic energy, which is shown in figure 5b, provides a concise quantification of the intensity of the turbulence, and increased within regime I, three- to fourfold at 7 m, 50 m and 100 m over an hour-long period from 10.30 CDT to 11.30 CDT as the convective eddies observed in figure 3a increased in intensity and introduced additional shearing and turbulence production. Note that the estimate of turbulent kinetic energy obtained by the sonic anemometer is likely to be an underestimate because of the inability of this sensor to measure the vertical component of the velocity fluctuations. As the turbulent kinetic energy increased, driven by large-scale convective events, there was additional shearing and vorticity introduced at the smaller scales of turbulence. As a result, the rate of dissipation of the turbulent kinetic energy due to viscous effects tended to increase alongside turbulent kinetic energy, as observed throughout regime I.

During regime II the conditions at the surface were in an approximately steady state and, although the buoyant production measured at 50 m and 100 m appears to have decreased, the corresponding turbulent kinetic energy remained near its maximum values. However, the

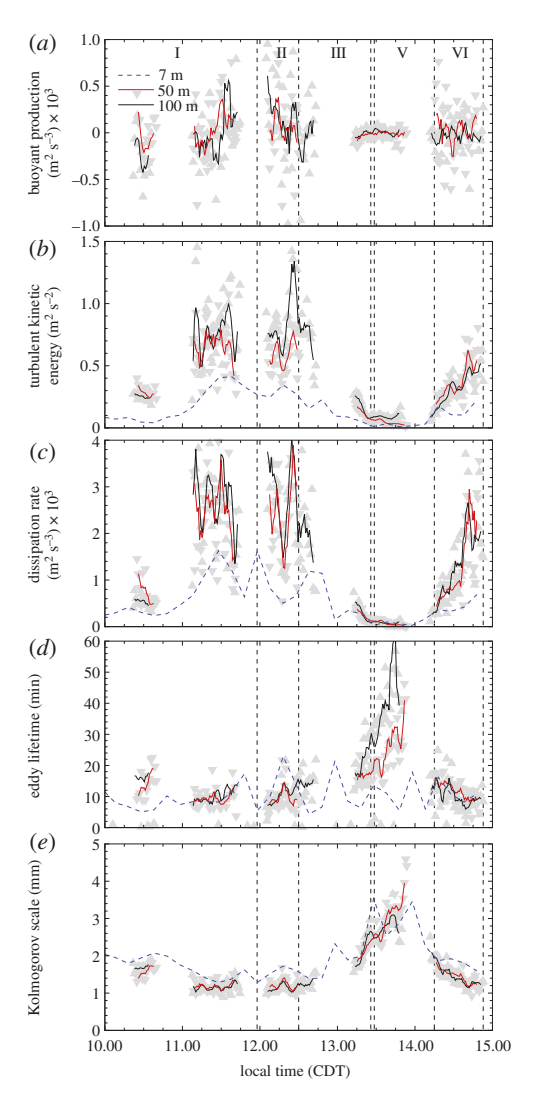


Figure 5. Time evolution of turbulence statistics measured at 7 m, 50 m and 100 m. (a) Buoyant production, B, calculated from fixed-wing aircraft flying at 50 m and 100 m. (b) Corresponding turbulent kinetic energy, k, compared with the estimated turbulent kinetic energy, k, measured by the sonic anemometer located at 7 m. (c) Turbulence dissipation rate, ϵ , estimated from the inertial subrange of the energy spectrum. (d) Eddy lifetime, defined as the ratio of the turbulent kinetic energy to the turbulence dissipation rate. (e) Kolmogorov scale, η , estimated from the turbulence dissipation rate and kinematic viscosity, describing the smallest scales of turbulence. Gray data points indicate statistics gathered from a single pass, with lines produced via a rolling average of five passes. Upward-pointing triangles indicate a measurement made at 100 m and downward-pointing triangles indicate a measurement made at 100 m and downward-pointing triangles indicate a measurement made at 50 m, with lines indicating the rolling average calculated from five successive passes. Data presented for the sonic anemometer at 7 m are calculated from 10 min averages with Taylor's hypothesis [70] used to estimate spatial information using the temporal variation. Vertical dashed lines indicate the boundaries between regimes with regimes identified by Roman numerals in (a). (Online version in colour.)

measurements at $7\,\mathrm{m}$ suggest that the turbulent kinetic energy at this height may have begun to decrease.

The decrease of insolation, and corresponding reduction in convective activity during regime III, resulted in the buoyant production at 50 m and 100 m becoming completely damped out by the inception of regime IV and the initiation of totality. Starved of additional turbulence by the drop in buoyant production, the turbulent kinetic energy experienced a corresponding decrease and is near zero by regime IV. Insulated from the surface-driven processes by the stable

layer which formed in regime V, a residual layer formed above the stable layer. As a result, the buoyant production, turbulent kinetic energy and its dissipation rate remained near zero until regime VI, at which point they began to recover as the insolation increased back to non-eclipse levels.

Given that the stable layer forming during regime V formed within the lowest 50 m (figure 4), it can be expected that the greatest damping of the turbulence would be within this lowest 50 m. Therefore, the reduction in turbulence at 50 m and 100 m is attributed to the lack of a production mechanism coupled with a high rate of dissipation. The residual layer conditions which formed above the stable layer were well mixed and, as a result, lack the mean temperature and humidity gradients required for buoyant and mechanical production of turbulence. Without a mechanism for sustaining its energy, the turbulence dissipation caused the turbulent kinetic energy to decay rapidly.

The eddy lifetime, shown in figure 5*d*, provides a coarse measure of the time it would take for the turbulent kinetic energy content at a particular location to decay without any additional energy addition. For most of regimes I–III, the eddy lifetime is of the order of 10 min, which is consistent with the observed rapid decay of turbulent kinetic energy caused by the drop in buoyant production during regime III. During regimes IV and V, an altitude dependence in eddy lifetime developed, produced by a small-altitude dependence in turbulent kinetic energy, most likely in the larger turbulent scales which are less constrained by proximity to the surface and decay more slowly. Within the stable layer, the eddy lifetime remains unchanged as there is suppression of the turbulent production. However, the slightly higher turbulent kinetic energy above 50 m caused an increase in eddy lifetime as the dissipation rate decreased.

When looking at the Kolmogorov scale behaviour during regimes III–V (figure 5*f*), we observed an increase in this scale that initiated at the start of regime III owing to the decay of turbulence during that regime. This growth in Kolmogorov scale continued until the latter portion of regime V, at which point it began to decrease again as the buoyant production resumed and injected more kinetic energy into the smaller scales.

(d) Atmospheric surface layer wind direction changes

One of the more inconsistently observed meteorological phenomena associated with the eclipse is the formation of an eclipse wind. It has previously been proposed that this wind is caused by the formation of a cold-core cyclone centred around the umbra due to localized cooling of the surface [20,21]. However, compelling evidence of the existence of this cyclone has been elusive. For example, Gray & Harrison [23] observed backing (anti-clockwise) change in the surface wind direction during the 1999 eclipse over Europe and attributed this phenomenon to the formation of a cold-core cyclone. However, they later revised this conclusion based on a later study of the 2015 eclipse over the British Isles [10], whereby similar backing of the surface winds was observed and attributed to the formation of a nocturnal jet. In this section, we look more closely at the changes in the wind speed and direction observed at the measurement site. To provide an initial overview, wind speed and direction results from different altitudes are presented in figure 6a–e, for each of the regimes identified in the previous sections.

During regimes I and II (figure 6a,b), the winds were from the southwest at approximately 210° and variable, consistent with the synoptic-scale winds with variability caused by convective boundary layer conditions. Between first and third contact, during regimes III and IV (figure 6c), as the decrease of insolation began to impact the atmospheric boundary layer and turbulent activity decreased, a large variation in wind direction was observed at all altitudes. The wind direction rotated clockwise (veered) by as much as 90° before returning to 230°, close to the original direction. The wind speed remained largely unchanged during the process at 50 m and 100 m, but dropped at 7 m and 3 m, as also observed in figure 2c. During regime V (figure 6d), during the formation of the stable layer, the winds were calm at the 3 m altitude, but at 50 m and 100 m remained near the pre-eclipse speed and direction. The variation in direction at 50 m and 100 m during regime V was much smaller than that during regimes I and II because of the

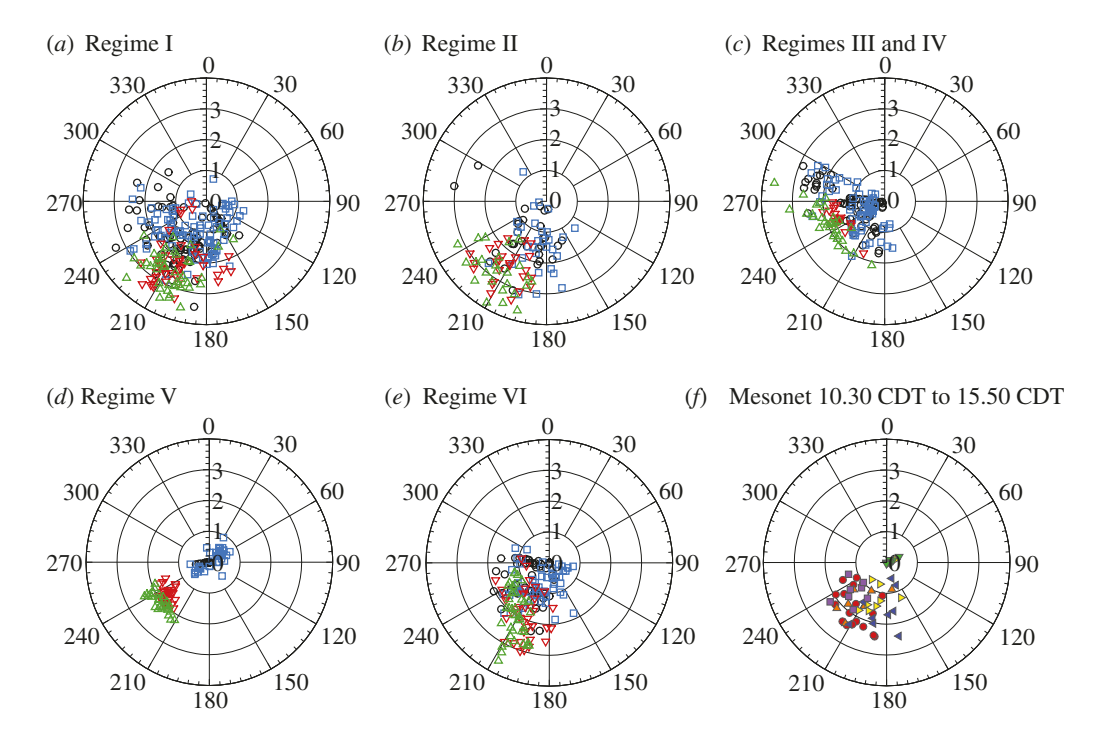


Figure 6. Wind speed and direction plots measured between 3 m and 100 m. Wind speed in m s⁻¹ and direction at Russellville—Logan County Airport measured at 3 m, 7 m, 50 m and 100 m during: (a) regime I; (b) regime II; (c) regimes III and IV; (d) regime V and (e) regime VI. Wind speed and direction for the same time period are presented in (f) at 10 m measured at Logan County Mesonet site (latitude 36.86, longitude —86.91, approx. 8.5 km from Russellville Airport). Data points from 3 m and 7 m from the cup and vane and sonic anemometer are shown at 1 min intervals. Data points from 50 m and 100 m are presented from the fixed-wing UAVs as an average for each transect (approx. 40 s intervals). Data points from the Logan County Mesonet site in (f) are presented at 5 min intervals. Direction is meteorological direction. In (a-e), symbols indicate the altitude of measurement with: black circles indicating 3 m; blue squares indicating 7 m; red inverted triangles indicating 50 m; and green triangles indicating 100 m. In (f), symbols indicate the time of measurement with: red circles indicating regime I; orange triangles indicating regime II; green inverted triangles indicating regimes IV and V; blue left pointed triangles indicating regime VI; and purple squares indicating measurements made after 15.00 CDT. (Online version in colour.)

suppression of turbulence production. As also observed in figure 2c the sonic anemometer at 7 m was able to pick up a $0.5\,\mathrm{m\,s^{-1}}$ wind; from figure 6d it is clearer that there was a variation in wind direction by 180° , consistent with the formation of wind shear within the stable layer as observed in figure 4c. During regime VI (figure 6e), as the temperature difference between the surface and atmosphere returned to pre-eclipse conditions, the wind speed and direction at all altitudes became similar to those observed in regimes I and II.

The greatest impact on the large-scale winds was observed during regime III, in the form of a 90° veering in direction. This is counter to the direction change expected to be associated with the formation of a nocturnal jet, but is potentially consistent with the passage of a large-scale cold-core cyclone past the measurement location of the form proposed by Aplin & Harrison [20]. However, if such were the case, the return to a synoptic-scale wind direction would be expected to occur in regimes V and VI, rather than during regime III. To investigate further, the wind speed and direction data from the Logan County Mesonet site are shown in figure 6f. The data from this site, located approximately 8.5 km from the Russellville Airport measurement site, show no commensurate variation in wind direction. This site reported surface wind directions consistently from the southwest throughout the day, although calming during regime IV while simultaneously

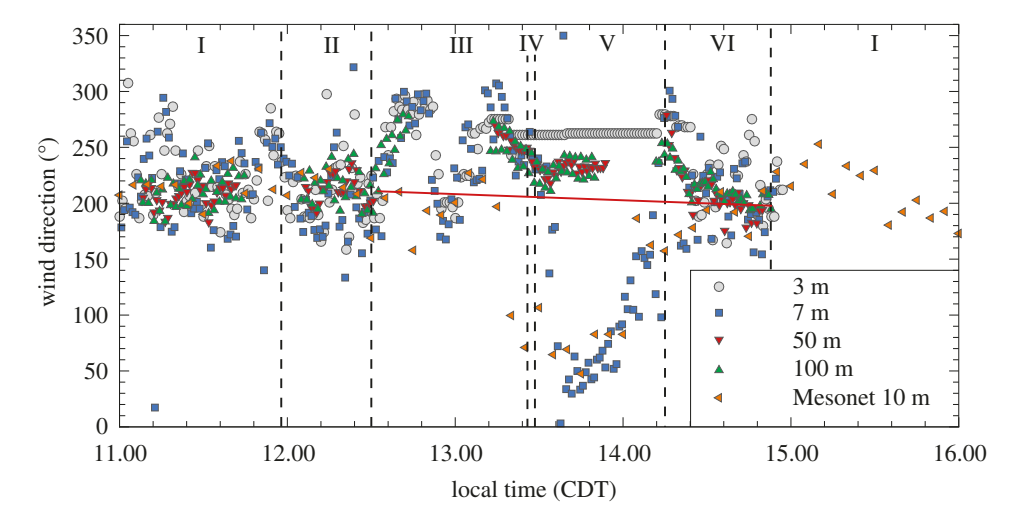


Figure 7. Wind direction measured at different altitudes. Wind direction measured at 3 m, 7 m, 50 m and 100 m at Russellville Airport and at 10 m at the Logan County Mesonet site during eclipse. Direction is meteorological direction. Values at 3 m and 7 m presented at 1 min intervals, Mesonet values presented at 5 min intervals, values at 50 m and 100 m presented as the average from each transect (approx. 40 s). Vertical dashed lines and Roman numerals indicate the regime; the red solid line indicates a 20° backing of the wind between regimes III and VI. (Online version in colour.)

backing 180° . This, therefore, suggests that the large wind direction change during regime III was a localized variation, potentially due to the large thermals observed in figures 3a and 4a. Therefore, although it is possible that a cold-core cyclone forms, its impact on the winds is not noticeable in the present data.

To examine the possibility of nocturnal jet formation, as proposed by Gray & Harrison [10], we isolated the wind direction changes during the eclipse in figure 7. Noticeable are the local veering of the wind in regime III and the 180° rotation of the surface winds during regime V. Also noticeable is the constant direction reported at 3 m as the wind magnitude dropped below the sensitivity of the anemometer located at that height.

Noting that the turbulent kinetic energy and corresponding thermals were suppressed during regimes III–VI, we infer that it is during these regimes that the atmospheric boundary layer is most likely to have decreased in depth and provide the conditions proposed to produce the nocturnal jet. Although the wind direction fluctuates significantly over these regimes, hidden within these fluctuations is evidence of a backing of the wind direction of 20° from the start of regime III to the end of regime VI. A red line in figure 7 has been added from 210° to 190° over this time period to highlight this wind direction change. Although this is not strong evidence in support of the observations made by Gray and Harrison, the same trend did appear in the measurements made at both Russellville Airport and the Logan County Mesonet site. This is emhasized by what appears to be recovery of the wind direction after the eclipse reported by the Mesonet site. Unfortunately, the measurements had concluded at the Russellville site at the end of regime VI.

We now focus on the 180° direction change measured during regimes IV and V. To investigate this direction change in greater detail, we present in figure 8 the profiles of the mean wind vectors measured at 1 m intervals during flights 10, 11 and 12 made by the rotorcraft, specifically those flights which occurred during regimes IV and V. The mean wind vectors measured during regime IV and at the start of regime V (figure 8a) show the initial influence of the stable layer formation as a decrease in wind speed below 40 m, but no change in direction is evident. During flight 11 (figure 8b), when the stable layer is most established, there is a noticeable backing of the wind vector between 10 m and 50 m, with the 180° reversal of the flow observed in the 7 m sonic tower also evident in the vectors closest to 10 m. This backing can be associated with

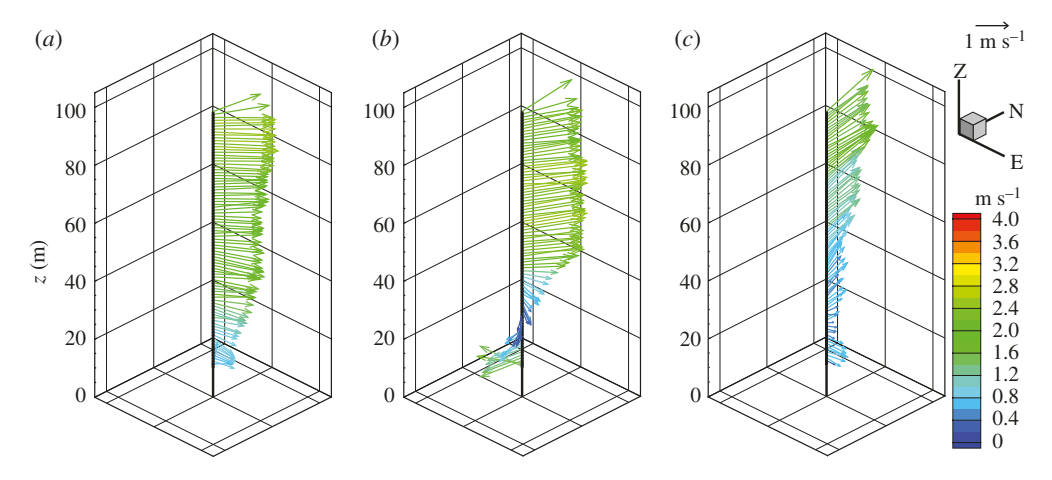


Figure 8. Mean wind vectors at 1 m intervals measured by rotorcraft during regimes IV and V. Wind vectors measured during (a) flight 10 (13:25 CDT–13:35 CDT), (b) flight 11 (13:42 CDT–13:52 CDT) and (c) flight 12 (13:53 CDT–14:02 CDT). Vectors averaged over the duration of the flight at 1 m intervals and shown coloured by magnitude of the vector with a 1 m s⁻¹ reference vector in the upper right. (Online version in colour.)

dynamic sinking of cold air during the eclipse event and could be interpreted as cyclonic activity. Interestingly, though, this rotation is confined to the stable layer, thus not supporting the cold-core cyclone model as proposed by Clayton [21]. Furthermore, the rotation around the horizontal axis appears much stronger than that around the vertical axis. Flight 12 (figure 8c) occurred towards the end of regime V as the stable layer weakened. Although the measured wind magnitude reduction extended to 80 m, the backing of the wind vector is still evident, although only in the lowest 20 m of the measurement, the approximate depth of the stable layer during that flight.

4. Conclusion

In summary, these UAV-enabled measurements provided unprecedented resolution of the atmospheric surface layer processes during a solar eclipse and thereby present a much more complete picture than previously held of the evolution of atmospheric surface layer behaviour during the corresponding rapid decrease and increase of insolation. Using the boundary conditions measured at the surface, six different regimes of behaviour were observed during the eclipse, which were particularly evident in the sensible heat flux. These regimes generally represent the different forms of response the surface layer has to the eclipse, and consist of typical diurnal evolution, damping of turbulent behaviour, formation of a stable nocturnal layer and recovery back to the typical diurnal evolution. Note that which regimes are observed at a particular location can be expected to vary depending on several factors, including: the time of day of the eclipse; time of the year; geography; and synoptic-scale weather. These factors will influence cloud cover, and relative surface and near-surface air temperature, which will produce different phenomenology and surface observations.

During the clear summer conditions which occurred during the observations described here, the most significant response was the formation of a temperature inversion and 50 m deep stable layer following totality, which thinned as the solar radiation increased and warmed the surface. Notably, the existence of this layer resulted in observations made at ground level being very different from observations made at altitude. Included in these observations was a strong backing of the wind vector by 180° within this layer, which is consistent with dynamic sinking of air towards the surface.

This formation of a stable layer near the surface bounded by a residual layer above was short-lived, lasting 45 min, and delayed by the retention of heat in the air until 15 min after totality.

Although previously suggested through indirect inference, e.g. through examination of stability parameters, in the present study, its formation was confirmed through direct observation. Given that the existence of this layer may only occur when the change in insolation due to the eclipse is large enough to support its formation, it is very likely that much of the variability in reported eclipse wind behaviour can be attributed to whether or not such a layer has formed.

The properties of the turbulence above the stable layer were influenced by the elimination of production mechanisms at the surface, resulting in a rapid decay of the turbulence throughout the measurement domain and the formation of a residual layer above the stable layer. The corresponding decrease in convective activity would be expected to cause the atmospheric boundary layer to become shallower, and some evidence of backing in the wind direction is present in the observations of wind direction, consistent with prior eclipse studies which attribute this to the formation of a corresponding nocturnal jet.

Data accessibility. Data are currently available through the following cloud storage link: https://www.dropbox.com/sh/qjt1tmpxtfemdqw/AABiwiuoDO9Mn8XzBoAzd_6Ha?dl=0.

Authors' contributions. A.L.H. and S.W.S. designed the study and managed the logistical organization. C.A.C. and M.P.S. conducted the measurements. S.C.C.B. performed the analysis. All authors contributed to the interpretation and preparation of the final manuscript.

Competing interests. We declare we have no competing interests.

Funding. This work was supported by the US National Science Foundation through award no. CBET-1351411 and by award no. 1539070, Collaboration Leading Operational UAS Development for Meteorology and Atmospheric Physics (CLOUDMAP).

Acknowledgements. The authors thank Ryan Nolin, Jonathan Hamilton, Robert Singler, Harrison Wight and Christina Vezzi, who maintained and flew the unmanned vehicles used in this study.

Appendix A. Post processing of data

Measured quantities were pressure in pascals, P, temperature in ${}^{\circ}$ C, relative humidity in ${}^{\circ}$ RH, and wind velocity components U(x,y,z,t), V(x,y,z,t) and W(x,y,z,t) in $m\,s^{-1}$ in the x, y and z directions, respectively. Here, unless mentioned otherwise, we will align x with the mean wind direction measured between 50 m and 100 m, z will be positive up away from the ground and y will be the remaining component parallel to the ground.

From the measured air temperature, the saturation pressure [71] was determined following:

$$P_s = \frac{\exp(77.345 + 0.0057(T + 273.15) - (7235)/(T + 273.15))}{(T + 273.15)^{8.2}},$$
 (A 1)

which was, in turn, used to calculate the partial pressure of the water vapour $P_v = (\%RH)P_s$ and the partial pressure of the dry air $P_d = P - P_v$. The density of the air could then be calculated using

$$\rho = \frac{P_d}{287.058 (T + 273.15)} + \frac{P_v}{461.495 (T + 273.15)}.$$
 (A 2)

In addition, the water vapour mixing ratio was determined as

$$q = 0.622 \frac{P_v}{P_d}. (A 3)$$

Dynamic viscosity of the air was found by first calculating the dynamic viscosity of the dry air

$$\mu_a = (0.40401 + 0.074582(T + 273.15) - 5.7171 \times 10^{-5}(T + 273.15)^2$$

$$+ 2.9928 \times 10^{-8}(T + 273.15)^3 - 6.2524 \times 10^{-12}(T + 273.15)^4) \times 10^{-6}$$
(A 4)

and then the dynamic viscosity of saturated air

$$\mu_v = \frac{T^{*-1/2}}{0.0181583 + 0.0177624T^* + 0.0105287T^{*2} - 0.0036744.*T^{*3}} \times 10^{-6},\tag{A 5}$$

where $T^* = 647.27/(T + 273.15)$.

These were combined to find the air viscosity following [72] and using

$$\mu = \frac{\mu_a}{1 + \Phi_{av} X_m} + \frac{\mu_v}{1 + \Phi_{va}/X_m},\tag{A 6}$$

where $X_m = 1.61q$,

$$\Phi_{av} = \frac{(1 + (\mu_a/\mu_v)^{1/2} (m_v/m_a)^{1/4})^2}{2^{3/2} (1 + m_a/m_v)^{1/2}}$$
(A 7)

and

$$\Phi_{va} = \frac{(1 + (\mu_v/\mu_a)^{1/2} (m_a/m_v)^{1/4})^2}{2^{3/2} (1 + m_v/m_a)^{1/2}}$$
(A 8)

with $m_a = 28.97$ being the molar mass of air and $m_v = 18.01528$ being the molar mass of water. With the dynamic viscosity and density known, the kinematic viscosity was calculated as $v = \mu/\rho$. In addition, the potential temperature

$$\theta = (T + 273.15) \frac{100\,000^{\,0.286}}{P} - 273.15 \tag{A 9}$$

and virtual potential temperature $\theta_v = (\theta + 273.15)(1 + 0.61q)$ could be calculated.

Unfortunately, the instrumentation available was insufficient to directly measure the different contributions to the surface energy balance. However, to gain a qualitative understanding of the contributions to the energy balance at the surface, and more specifically the sensible heat flux, which has been found to change significantly during eclipse events, the following simplified analysis was performed. The components of the surface energy balance [2,73] are given as

$$-Q_s^* = Q_H + Q_E + Q_G + \Delta Q_s,$$
 (A 10)

where Q_s^* is the net radiation at the surface, Q_H and Q_E are the turbulent sensible and latent heat fluxes, Q_G is the heat flux into the soil and ΔQ_s is the energy storage. Furthermore, the net radiation can be divided into longwave and shortwave contributions,

$$Q_s^* = K_{up} + K_{down} + I_{up} + I_{down},$$
 (A 11)

where $K_{\rm up}$ is the shortwave upwelling radiation, $K_{\rm down}$ is the shortwave downwelling radiation, $I_{\rm up}$ is the longwave upwelling radiation and $I_{\rm down}$ is the longwave downwelling radiation. Although all these components were not measured directly, an estimate of some of these contributions over the course of the day can be made using some simplifying assumptions. Using the parameterization provided by Burridge & Gadd [74] of

$$I_{\rm up} + I_{\rm down} = 0.08 \rho c_P (1 - \sigma_{cH} - 0.3 \sigma_{cM} - 0.6 \sigma_{cL}),$$
 (A 12)

where c_P is the specific heat at constant pressure, and σ_{cH} , σ_{cM} and σ_{cL} are the cloud cover at high, middle and low altitudes, respectively, which allows an estimate of constant $I_{\rm up} + I_{\rm down}$ to be made by letting $\sigma_{cH} = \sigma_{cM} = \sigma_{cL} \approx 0$ as the day was virtually cloudless. This allows Q_s^* to be estimated from the measured $K_{\rm down}$ if we assume an albedo of 0.2, typical for grass, such that $K_{\rm up} \approx 0.2 K_{\rm down}$.

Using the Boussinesq hypothesis

$$Q_H = -\rho c_P K_H \frac{\partial T}{\partial z},\tag{A 13}$$

the turbulent sensible heat flux could be estimated, where K_H is the eddy diffusivity and $\partial T/\partial z$ is the vertical temperature gradient at the surface. The temperatures measured at the surface and by the portable weather station provide a measure of the change in $\partial T/\partial z$ during the day; however, K_H remains an unknown. Furthermore, the accuracy of the measured moisture content was insufficient to allow recovery of the equivalent moisture gradient, and therefore we assume

 $Q_E = Q_H/Bo$, where Bo is the Bowen ratio. The heat flux into the soil can be found from the soil temperature measurements using

$$Q_G = k_G \frac{\partial T}{\partial z},\tag{A 14}$$

where k_G is the thermal conductivity of the soil.

Thus, an estimate of the contributions to equation (A 10) can be found if the three unknowns, K_H , k_G and ΔQ_s , can be approximated. Soil and air temperatures reached steady-state conditions twice during the measurement, shortly after first contact and shortly after third contact. At these times $\Delta Q_s \approx 0$, and therefore we can use the measured values of $\partial T/\partial z$ and solar radiation at these two times to solve for K_H and k_G , allowing the estimate of the evolution of Q_H and Q_G during the eclipse. Note that a value of Bo = 0.75 was assumed for the time near first contact and Bo = -1.5 for the time near third contact [61]; however, the results were found to be relatively insensitive to the actual value of Bo used. Note also that the assumption of constant K_H is likely to be a gross oversimplification given the significant changes observed in the surface layer turbulence which were observed during the eclipse event.

The rotorcraft data were processed in two ways. The first was to generate mean profiles of T(x,y,z,t), $\theta(x,y,z,t)$, U(x,y,z,t), etc. as a function of z only. This was done for each flight by averaging all data acquired within z = 1 m intervals.

The data from this system were also processed to produce time series of T(x, y, z, t), $\theta(x, y, z, t)$, etc. as a function of z and t only. To do this, we averaged successive ascent/descent and descent/ascent pairs within z = 1 m intervals, and then interpolated between these intervals in time using a piecewise spline interpolation function.

To calculate turbulence statistics from the fixed-wing aircraft, we divided each flight into individual transects or passes. For each pass, the x-component of the coordinate system was first rotated to align with the mean wind direction for that transect. Then, the fluctuating components of wind velocity and θ were calculated according to $u(x,y,z,t) = U(x,y,z,t) - \langle U \rangle$, with the same calculations performed to find v(x,y,z,t) and w(x,y,z,t) and $\theta'(x,y,z,t) = \theta(x,y,z,t) - \langle \theta \rangle$. Here, $\langle U \rangle$ is the linear trend of U(x,y,z,t) measured during the transect, and hence contributions to u(x,y,z,t), v(x,y,z,t), w(x,y,z,t) and $\theta'(x,y,z,t)$ from wavelengths longer than approximately 1600 m are necessarily filtered out. The variance and covariance of these terms were then calculated according to

$$\overline{uv} = \frac{1}{N} \sum_{n=1}^{N} u_n(x, y, z, t) v_n(x, y, z, t),$$
(A 15)

where n are the discrete samples of u and v measured along the transect and N is the total number of samples acquired along the transect. The overline here is used to indicate a quantity averaged over a single transect. A similar process was used to calculate $\overline{u^2}$, $\overline{v^2}$, \overline{uw} , \overline{vw} , $\overline{u\theta'}$, $\overline{v\theta'}$ and $\overline{w\theta'}$.

With the Reynolds stresses calculated, the turbulent kinetic energy, $\overline{k} = 1/2(\overline{u^2} + \overline{v^2} + \overline{w^2})$ and buoyant production $B = 9.81/(\overline{\theta_v} \ \overline{w\theta'})$ could be readily calculated.

Power spectra and autocorrelations were also calculated [75]. To do this, the coordinate system was rotated such that x was aligned with the direction of flight. To simplify the calculation, the measurements made along the transect were interpolated onto regularly spaced locations along the flight path. This allowed transformation of u(x) using a fast Fourier transform to obtain $F(1/\lambda)$, where λ is the wavelength in the x-direction. In turn, this was transformed to wavenumber space such that $\kappa = 2\pi/\lambda$ and the power spectrum $P(\kappa) = |F(\kappa)|^2$ and scaled such that

$$\overline{u^2} = \int P(\kappa) \, \mathrm{d}\kappa. \tag{A 16}$$

The inverse fast Fourier transform was then used to produce the autocorrelation and the longitudinal integral scale, L_{11} , found by integrating the autocorrelation to the first zero crossing.

With the power spectrum and autocorrelation calculated, the dissipation rate was estimated using a two-step process. The first step assumed that the entire measured spectrum was within

the inertial subrange, allowing a first estimate of ε using the Kolmogorov theory [76]

$$\varepsilon = \frac{1}{N} \sum_{1}^{N} \left(\frac{P(\kappa) \kappa^{5/3}}{0.49} \right)^{3/2},\tag{A 17}$$

where N is the number of discrete points in the calculated $P(\kappa)$. A first estimate of the Kolmogorov scale $\eta = (v^3/\varepsilon)^{1/4}$ could then be found. Using this value, a more precise estimate of ε and η could be found by repeating this calculation using only points in the power spectrum falling within the range $0.005 > \kappa \eta > 0.0001$, which will be within the inertial subrange for the Reynolds numbers of the atmospheric turbulence observed during these measurements.

The same procedures were used to calculate the statistics measured by the sonic anemometer at 7 m, with the following modifications. First, the time series was divided into 10 min intervals and Taylor's frozen flow hypothesis [70] was used to transform from the temporal domain to the spatial domain using the mean wind speed for each interval. Given that the mean wind speed was typically $2 \,\mathrm{m\,s^{-1}}$, a 10 min interval corresponds to 1200 m of data, roughly equivalent to a single transect of the fixed-wing aircraft. In addition, since the W component of velocity was not available, the turbulent kinetic energy was approximated as $\tilde{k} \approx 0.5(1.5u^2 + 1.5v^2)$. Note that in the predominantly convective conditions occurring during these measurements \tilde{k} can be expected to be significantly lower than k.

References

- 1. Walker G. 2008 An ocean of air: a natural history of the atmosphere. London, UK: Bloomsbury.
- 2. Foken T. 2008 Micrometeorology. Berlin, Germany: Springer.
- 3. Brown GL, Roshko A. 1974 On density effects and large structure in turbulent mixing layers. J. Fluid Mech. 64, 775–816. (doi:10.1017/S002211207400190X)
- 4. Gao W, Shaw RH, Paw U KT. 1989 Observation of organized structure in turbulent flow within and above a forest canopy. *Bound. Layer Meteorol.* **59**, 35–57. (doi:10.1007/BF00120685)
- 5. Kapoor RK, Adiga BB, Singal SP, Aggarwal SK, Gera BS. 1982 Studies of the atmospheric stability characteristics during the solar eclipse of February 16, 1980. *Bound. Layer Meteorol.* 24, 415–419. (doi:10.1007/BF00120730)
- Eaton FD, Hines JR, Hatch WH, Cionco RM, Byers J, Garvey D, Miller DR. 1997 Solar eclipse effects observed in the planetary boundary layer over a desert. *Bound. Layer Meteorol.* 83, 331–346. (doi:10.1023/A:1000219210055)
- 7. Girard-Ardhuin F, Bénech B, Campistron B, Dessens J, Jacoby-Koaly S. 2003 Remote sensing and surface observations of the response of the atmospheric boundary layer to a solar eclipse. *Bound. Layer Meteorol.* **106**, 93–115. (doi:10.1023/A:1020837400800)
- 8. Amiridis V *et al.* 2007 Aerosol Lidar observations and model calculations of the Planetary Boundary Layer evolution over Greece, during the March 2006 Total Solar Eclipse. *Atmos. Chem. Phys.* 7, 6181–6189. (doi:10.5194/acp-7-6181-2007)
- 9. Bala Subrahamanyam D, Anurose TJ, Mohan M, Santosh M, Kiran Kumar NVP, Sijikumar S, Prijith SS, Aloysius M. 2011 Atmospheric surface-layer response to the annular solar eclipse of 15 January 2010 over Thiruvananthapuram, India. *Bound. Layer Meteorol.* **141**, 325. (doi:10.1007/s10546-011-9627-z)
- 10. Gray SL, Harrison RG. 2016 Eclipse-induced wind changes over the British Isles on the 20 March 2015. *Phil. Trans. R. Soc. A* 374, 20150224. (doi:10.1098/rsta.2015.0224)
- 11. Edward H. 2000 Meteorological effects of the solar eclipse of 11 August 1999. Weather 55, 430–446. (doi:10.1002/wea.2000.55.issue-12)
- Winkler P, Kaminski U, Köhler U, Riedl J, Schroers H, Anwender D. 2001 Development of meteorological parameters and total ozone during the total solar eclipse of August 11, 1999. *Meteorol. Z.* 10, 193–199. (doi:10.1127/0941-2948/2001/0010-0193)
- 13. Foken T, Wichura B, Klemm O, Gerchau J, Winterhalter M, Weidinger T. 2001 Micrometeorological measurements during the total solar eclipse of August 11, 1999. *Meteorol. Z.* **10**, 171–178. (doi:10.1127/0941-2948/2001/0010-0171)
- 14. Founda D, Melas D, Lykoudis S, Lisaridis I, Gerasopoulos E, Kouvarakis G, Petrakis M, Zerefos C. 2007 The effect of the total solar eclipse of 29 March 2006 on meteorological variables in Greece. *Atmos. Chem. Phys.* **7**, 5543–5553. (doi:10.5194/acp-7-5543-2007)

- 15. Kameda T, Fujita K, Sugita O, Hirasawa N, Takahashi S. 2009 Total solar eclipse over Antarctica on 23 November 2003 and its effects on the atmosphere and snow near the ice sheet surface at Dome Fuji. *J. Geophys. Res. Atmos.* **114**, D18115. (doi:10.1029/2009JD011886)
- 16. Kastendeuch PP, Najjar G, Colin J, Luhahe R, Bruckmann F. 2016 Effects of the 20 March 2015 solar eclipse in Strasbourg, France. *Weather* 71, 55–62. (doi:10.1002/wea.2016.71.issue-3)
- 17. Krishnan P, Kunhikrishnan PK, Nair SM, Ravindran S, Ramachandran R, Subrahamanyam DB, Venkata Ramana M. 2004 Observations of the atmospheric surface layer parameters over a semi arid region during the solar eclipse of August 11th, 1999. *J. Earth Syst. Sci.* 113, 353–363. (doi:10.1007/BF02716730)
- 18. Raman S, Boone P, Rao KS. 1990 Observations and numerical simulation of the evolution of the tropical planetary boundary layer during total solar eclipses. *Atmos. Environ. Part A. Gen. Top.* **24**, 789–799. (doi:10.1016/0960-1686(90)90279-V)
- 19. Anderson RC, Keefer DR. 1975 Observation of the temperature and pressure changes during the 30 June 1973 solar eclipse. *J. Atmos. Sci.* **32**, 228–231. (doi:10.1175/1520-0469(1975) 032<0228:OOTTAP>2.0.CO;2)
- 20. Aplin K, Harrison R. 2003 Meteorological effects of the eclipse of 11 August 1999 in cloudy and clear conditions. *Proc. R. Soc. Lond. A* **459**, 353–371. (doi:10.1098/rspa.2002.1042)
- 21. Clayton HH. 1901 The eclipse cyclone of 1900. Q. J. R. Meteorol. Soc. 29, 47–53. (doi:10.1002/qj.49702912507)
- 22. Prenosil T. 2000 The influence of the 11 August 1999 total solar eclipse on the weather over central Europe. *Meteorol. Z.* **9**, 351–359. (doi:10.1127/metz/9/2000/351)
- 23. Gray SL, Harrison RG. 2012 Diagnosing eclipse-induced wind changes. *Proc. R. Soc. A* 468, 1839–1850. (doi:10.1098/rspa.2012.0007)
- 24. Antonia R, Chambers A, Phong-Anant D, Rajagopalan S, Sreenivasan K. 1979 Response of atmospheric surface-layer turbulence to a partial solar eclipse. *J. Geophys. Res. Oceans Atmos.* 84, 1689–1692. (doi:10.1029/JC084iC04p01689)
- Gorchakov GI, Kadygrov EN, Kortunova ZV, Isakov AA, Karpov AV, Kopeikin VM, Miller EA. 2008 Eclipse effects in the atmospheric boundary layer. *Izvestiya. Atmos. Ocean. Phys.* 44, 100–106. (doi:10.1134/S0001433808010118)
- 26. Gerasopoulos E *et al.* 2008 The total solar eclipse of March 2006: overview. *Atmos. Chem. Phys.* **8**, 5205–5220. (doi:10.5194/acp-8-5205-2008)
- 27. Anfossi D, Schayes G, Degrazia G, Goulart A. 2004 Atmospheric turbulence decay during the solar total eclipse of 11 August 1999. *Bound. Layer Meteorol.* **111**, 301–311. (doi:10.1023/B:BOUN.0000016491.28111.43)
- 28. Jayakrishnan P, Babu C, Sivaprasad P. 2013 Drastic variation in the surface boundary layer parameters over Cochin during the annular solar eclipse: analysis using sonic anemometer data. *J. Atmos. Sol. Terr. Phys.* **94**, 49–53. (doi:10.1016/j.jastp.2012.12.019)
- 29. Payne F, Lumley J. 1966 One-dimensional spectra derived from an airborne hot-wire anemometer. Q. J. R. Meteorol. Soc. 92, 397–401. (doi:10.1002/(ISSN)1477-870X)
- 30. Lenschow D, Johnson W. 1968 Concurrent airplane and balloon measurments of atmospheric boundary layer structure over a forest. *J. Appl. Meteor.* 7, 79–89. (doi:10.1175/1520-0450(1968)007<0079:CAABMO>2.0.CO;2)
- 31. Sheih CM, Tennekes H, Lumley J. 1971 Airborne hot-wire measurements of the small-scale structure of atmospheric turbulence. *Phys. Fluids* 14, 201–215. (doi:10.1063/1.1693416)
- 32. Eberhard W, Cupp R, Healey K. 1989 Doppler lidar measurement of profiles of turbulence and momentum flux. *J. Atmos. Ocean. Technol.* **6**, 809–819. (doi:10.1175/1520-0426(1989) 006<0809:DLMOPO>2.0.CO;2)
- 33. Angevine W, Avery S, Kok J. 1993 Virtual heat flux measurements from a boundary-layer profiler-RASS compared to aircraft measurements. *J. Appl. Meteor.* **32**, 1901–1907. (doi:10.1175/1520-0450(1993)032<1901:VHFMFA>2.0.CO;2)
- 34. Wood R, Stromberg IM, Jonas PR, Mill CS. 1997 Analysis of an air motion system on a light aircraft for boundary layer research. *J. Atmos. Oceanic Technol.* **14**, 960–968. (doi:10.1175/1520-0426(1997)014<0960:AOAAMS>2.0.CO;2)
- 35. Philbrick CR. 2002 Raman lidar techniques applied to meteorological sensing. In *Proc. Annu. Meeting of the American Meteorological Society, Sixth Symposium on Integrated Observing Systems, Orlando, FL, 12–17 January 2002*, pp. 1–9. Boston, MA: AMS.
- 36. Cho JYN, Newell RE, Anderson BE, Barrick JDW, Thornhill KL. 2003 Characterizations of tropospheric turbulence and stability layers from aircraft observations. *J. Geophy. Res. Atmos.* **108**, 8784. (doi:10.1029/2002JD002820)

- 37. Kalogiros JA, Wang Q. 2002 Calibration of a radome-differential GPS system on a Twin Otter research aircraft for turbulence measurements. *J. Atmos. Oceanic Technol.* **19**, 159–171. (doi:10.1175/1520-0426(2002)019<0159:COARDG>2.0.CO;2)
- 38. Kalogiros JA, Wang Q. 2002 Aerodynamic effects on wind turbulence measurements with research aircraft. *J. Atmos. Oceanic Technol.* **19**, 1567–1576. (doi:10.1175/1520-0426(2002) 019<1567:AEOWTM>2.0.CO;2)
- 39. Matvev V, Dayan U, Tass I, Peleg M. 2002 Atmospheric sulfur flux rates to and from Israel. *Sci. Total Environ.* **291**, 143–154. (doi:10.1016/S0048-9697(01)01089-0)
- 40. LeMone MA, Grossman RL, Chen F, Ikeda K, Yates D. 2003 Choosing the averaging interval for comparison of observed and modeled fluxes along aircraft transects over a heterogeneous surface. *J. Hydrometeorol.* **4**, 179–195. (doi:10.1175/1525-7541(2003)4<179:CTAIFC>2.0.CO;2)
- 41. Kalogiros J, Wang Q. 2011 Aircraft observations of sea-surface turbulent fluxes near the California coast. *Bound. Layer Meteorol.* **139**, 283–306. (doi:10.1007/s10546-010-9585-x)
- 42. Vellinga OS, Dobosy RJ, Dumas EJ, Gioli B, Elbers JA, Hutjes RWA. 2013 Calibration and quality assurance of flux observations from a small research aircraft. *J. Atmos. Oceanic Technol.* **30**, 161–181. (doi:10.1175/JTECH-D-11-00138.1)
- 43. Zulueta RC, Oechel WC, Verfaillie JG, Hastings SJ, Gioli B, Lawrence WT, Paw UKT. 2013 Aircraft regional-scale flux measurements over complex landscapes of mangroves, desert, and marine ecosystems of Magdalena Bay, Mexico. *J. Atmos. Oceanic Technol.* 30, 1266–1294. (doi:10.1175/JTECH-D-12-00022.1)
- 44. Mallaun C, Giez A, Baumann R. 2015 Calibration of 3-D wind measurements on a single-engine research aircraft. *Atmos. Meas. Technol.* **8**, 3177–3196. (doi:10.5194/amt-8-3177-2015)
- 45. Metzger S, Junkermann W, Butterbach-Bahl K, Schmid HP, Foken T. 2011 Measuring the 3-D wind vector with a weight-shift microlight aircraft. *Atmos. Meas. Technol.* 4, 1421–1444. (doi:10.5194/amt-4-1421-2011)
- 46. de Boer G *et al.* 2018 A birds-eye view: development of an operational arm unmanned aerial capability for atmospheric research in Arctic Alaska. *Bull. Am. Meteorol. Soc.* **99**, 1197–1212. (doi:10.1175/BAMS-D-17-0156.1)
- 47. Kral S *et al.* 2018 Innovative strategies for observations in the Arctic atmospheric boundary layer (ISOBAR)—the Hailuoto 2017 campaign. *Atmosphere* **9**, 268. (doi:10.3390/atmos9070268)
- 48. Bonin T, Chilson P, Zielke B, Fedorovich E. 2013 Observations of the early evening boundary-layer transition using a small unmanned aerial system. *Bound. Layer Meteorol.* **146**, 119–132. (doi:10.1007/s10546-012-9760-3)
- 49. Wildmann N, Rau GA, Bange J. 2015 Observations of the early morning boundary-layer transition with small remotely-piloted aircraft. *Bound. Layer Meteorol.* **157**, 345–373. (doi:10.1007/s10546-015-0059-z)
- 50. Lothon M *et al.* 2014 The BLLAST field experiment: boundary-layer late afternoon and sunset turbulence. *Atmos. Chem. Phys.* **14**, 10931–10960. (doi:10.5194/acp-14-10931-2014)
- 51. Cassano JJ, Maslanik JA, Zappa CJ, Gordon AL, Cullather RI, Knuth SL. 2010 Observations of Antarctic polynya with unmanned aircraft systems. *Eos Trans. Am. Geophys. Union* **91**, 245–246. (doi:10.1029/2010EO280001)
- 52. Van den Kroonenberg A, Martin T, Buschmann M, Bange J, Vörsmann P. 2008 Measuring the wind vector using the autonomous mini aerial vehicle M2AV. *J. Atmos. Ocean. Technol.* **25**, 1969–1982. (doi:10.1175/2008]TECHA1114.1)
- 53. van den Kroonenberg A, Bange J. 2007 Turbulent flux calculation in the polar stable boundary layer: multiresolution flux decomposition and wavelet analysis. *J. Geophys. Res. Atmos.* **112**, D06112. (doi:10.1029/2006ID007819)
- 54. Schuyler TJ, Guzman MI. 2017 Unmanned aerial systems for monitoring trace tropospheric gases. *Atmosphere* **8**, 206. (doi:10.3390/atmos8100206)
- 55. Platis A, Altstädter B, Wehner B, Wildmann N, Lampert A, Hermann M, Birmili W, Bange J. 2016 An observational case study on the influence of atmospheric boundary-layer dynamics on new particle formation. *Bound. Layer Meteorol.* **158**, 67–92. (doi:10.1007/s10546-015-0084-y)
- 56. Corrigan C, Roberts G, Ramana M, Kim D, Ramanathan V. 2008 Capturing vertical profiles of aerosols and black carbon over the Indian Ocean using autonomous unmanned aerial vehicles. *Atmos. Chem. Phys.* 8, 737–747. (doi:10.5194/acp-8-737-2008)
- 57. Ramanathan V, Ramana MV, Roberts G, Kim D, Corrigan C, Chung C, Winker D. 2007 Warming trends in Asia amplified by brown cloud solar absorption. *Nature* **448**, 575–578. (doi:10.1038/nature06019)

- 58. Balsley BB, Lawrence DA, Woodman RF, Fritts DC. 2013 Fine-scale characteristics of temperature, wind, and turbulence in the lower atmosphere (0–1,300 m) over the south Peruvian coast. *Bound. Layer Meteorol.* **147**, 165–178. (doi:10.1007/s10546-012-9774-x)
- 59. Witte BM, Singler RF, Bailey SC. 2017 Development of an unmanned aerial vehicle for the measurement of turbulence in the atmospheric boundary layer. *Atmosphere* **8**, 195. (doi:10.3390/atmos8100195)
- 60. Turner DD, Wulfmeyer V, Behrendt A, Bonin TA, Choukulkar A, Newsom RK, Brewer WA, Cook DR. 2018 Response of the land-atmosphere system over north-central oklahoma during the 2017 eclipse. *Geophys. Res. Lett.* **45**, 1668–1675. (doi:10.1002/grl.v45.3)
- 61. Wood JD *et al.* 2019 Land-atmosphere responses to a total solar eclipse in three ecosystems with contrasting structure and physiology. *J. Geophys. Res. Atmos.* **124**, 530–543. (doi:10.1029/2018JD029630)
- 62. Fowler J, Wang J, Ross D, Colligan T, Godfrey J. 2019 Measuring ARTSE2017: results from Wyoming and New York. *Bull. Am. Meteorol. Soc.* **100**, 1049–1060. (doi:10.1175/BAMS-D-17-0331.1)
- 63. Buban MS, Lee TR, Dumas EJ, Baker CB, Heuer M. 2019 Observations and numerical simulation of the effects of the 21 August 2017 North American total solar eclipse on surface conditions and atmospheric boundary-layer evolution. *Bound. Layer Meteorol.* **171**, 257–270. (doi:10.1007/s10546-018-00421-4)
- 64. Treaster AL, Yocum AM. 1978 The calibration and application of five-hole probes. Technical Report TM 78-10. See https://apps.dtic.mil/dtic/tr/fulltext/u2/a055870.pdf.
- 65. Wildmann N, Hofsäß M, Weimer F, Joos A, Bange J. 2014 MASC—a small remotely piloted aircraft (RPA) for wind energy research. *Adv. Sci. Res.* 11, 55–61. (doi:10.5194/asr-11-55-2014)
- 66. Bohn D, Simon H. 1975 Mehrparametrige Approximation der Eichräume und Eichflächen von Unterschall-bzw. Überschall-5-Loch-Sonden. *tm-Technisches Messen* 468, 81–89.
- 67. Axford DN. 1968 On the accuracy of wind measurements using an inertial platform in an aircraft, and an example of a measurement of the vertical mesostructure of the atmosphere. *J. Appl. Meteorol.* 7, 645–666. (doi:10.1175/1520-0450(1968)007<0645:OTAOWM>2.0.CO;2)
- 68. Lenschow D. 1972 The measurement of air velocity and temperature using the NCAR Buffalo aircraft measuring system. Technical Note NCAR-TN/EDD-74. Boulder, CO: National Center for Atmospheric Research.
- 69. Broxmeyer C, Leondes CI. 1964 Inertial navigation systems. *J. Appl. Mech.* 31, 735. (doi:10.1115/1.3629763)
- 70. Taylor GI. 1938 The spectrum of turbulence. *Proc. R. Soc. Lond. A* **164**, 476–490. (doi:10.1098/rspa.1938.0032)
- 71. Cengel YA, Boles MA. 2002 Thermodynamics: an engineering approach. New York, NY: McGraw-Hill Education.
- 72. Wilke CR. 1950 A viscosity equation for gas mixtures. *J. Chem. Phys.* **18**, 517–519. (doi:10.1063/1.1747673)
- 73. Stull R. 1988 An introduction to boundary layer meteorology. Berlin, Germany: Springer.
- 74. Burridge D, Gadd A. 1974 *The meteorological office operational 10-level numerical weather prediction model.* Technical Report Nos. 12 and 48. London, UK: HMSO.
- 75. Bendat JS, Piersol AG. 2000 Random data: analysis and measurement procedures, 3rd edn. New York, NY: Wiley Interscience.
- 76. Pope SB. 2000 Turbulent flows. Cambridge, UK: Cambridge University Press.